RESEARCH PAPER

The morphology of mass selected ruthenium nanoparticles from a magnetron-sputter gas-aggregation source

**R. M. Nielsen · S. Murphy · C. Strebel ·
M. Johansson · I. Chorkendorff · J. H. Nielsen**

Abstract We have investigated the morphology of mass selected ruthenium nanoparticles produced with a magnetron-sputter gas-aggregation source. The nanoparticles are mass selected using a quadrupole mass filter, resulting in narrow size distributions and average diameters between 2 and 15 nm. The particles are imaged in situ by scanning electron microscopy and scanning tunneling microscopy (STM) as well as ex-situ using transmission electron microscopy (TEM). For each distribution of mass selected nanoparticles, the height determined by STM and the width determined by TEM are seen to be similar throughout the mass range investigated. The particles are found to have a well-defined morphology for diameters below approximately 6 nm. Larger nanoparticles are less well-defined having rough surfaces, unlike the equilibrium morphology determined from the Wulff construction. The morphology of the particles is, in general, believed to be determined by the conditions inside the gas-aggregation source and the morphology is retained as the particles are soft-landed on the substrate.

R. M. Nielsen · S. Murphy · C. Strebel ·
M. Johansson · I. Chorkendorff · J. H. Nielsen (✉)
Center for Individual Nanoparticle Functionality,
Department of Physics, Nano-DTU, Technical University
of Denmark, 2800 Kgs. Lyngby, Denmark
e-mail: jane@fysik.dtu.dk
URL: www.cinf.dtu.dk

Introduction

Heterogeneous catalysts typically comprise the catalyst material distributed as nanoparticles on a high surface area support. This is a matter of twin considerations; first, the catalyst material is often costly and so the most efficient loading is sought and second, the nanosized particles often display superior catalytic behavior compared to the bulk material.

A range of intriguing examples exist where the catalytic properties depend strongly on morphological parameters such as the shape and the size of the nanoparticles. This includes, e.g., studies of gold nanoparticles for CO oxidation by O_2 (Haruta et al. 1989; Sanchez et al. 1999; Valden et al. 1998; Zanella et al. 2004; Janssens et al. 2007; Kung et al. 2007) and CO electrooxidation on gold clusters (Geng and LuG 2007) where strong size dependencies are observed. Several other transition metal nanoparticle systems have been investigated, focusing, e.g., on the size dependence of CO related surface reactivity on Rh (Frank and Bäumer 2000),

Pd (Wörz et al. 2003), Pt (Croy et al. 2007), Ni (Andersson et al. 2008), and Co nanoparticles (den Breejen et al. 2009). Also, the effect of shape of the nanoparticles has been under investigation, e.g., the methanol activity of supported Cu nanoparticles (Grunwaldt et al. 2000, Hansen et al. 2002) or the electro-oxidation activity from Pt nanocrystals (Tian et al. 2007).

In general, the catalytic activity of a surface is determined by the electronic structure of the surface atoms, and this is influenced by the local atomic structure. Changes in the number of neighbors or in the interatomic distance will, e.g., give rise to a change in the electronic structure. This is described in the d-band model (Hammer and Norskov 2000). The geometry of the surface site may also influence the catalytic activity by affecting the ability of the site to accommodate molecules or molecular fragments in an energetically favorable way (Dahl et al. 1999). As the size of a catalytic particle is changed, the availability of surface geometries changes, and the reaction rate of structure sensitive catalytic reactions can hence be strongly dependent on the size of the particles, both in the non-scalable ($< \sim 2$ nm) and scalable ($> \sim 2$ nm) regimes (Jacobsen et al. 2000; Silvestre-Albero et al. 2006; Landman et al. 2007; Andersson et al. 2008; Nørskov et al. 2008). For the purpose of studying these size effects using surface science techniques, a good representation is obtained by preparing an ensemble of monodisperse nanoparticles supported on a flat, crystallographically oriented, and well-defined substrate. Such model systems can give new insight into how the catalytic activity is influenced by the particle size and shape as well as by the support material.

Our goal is to establish a correlation between structure and activity in nanoparticulate catalysts. In this article, we study the morphology of a model catalyst comprising an ensemble of monodisperse ruthenium nanoparticles deposited onto a highly ordered pyrolytic graphite (HOPG) surface under ultrahigh vacuum (UHV) conditions. Ruthenium is a versatile catalyst with applications in the synthesis of methane through the methanation process (King 1978) as well as in the steam-reforming process (Jones et al. 2008). It has been found that the dissociation of CO, a key step in the methanation reaction, only occurs on the step sites of the ruthenium surface (Shincho et al. 1985; Zubkov et al. 2002; Zubkov et al. 2003). Ruthenium has also been put forward as an alternative to iron as a catalyst for ammonia synthesis, particularly at high ammonia concentrations (see Bielawa et al. 2001; Honkala et al. 2005 and references therein). The interaction of N_2 with ruthenium, which is believed to be the rate-limiting step in ammonia synthesis has therefore been a subject of fundamental interest. Nanoparticles of ruthenium on HOPG has, e.g., been investigated for the N_2 adsorption and desorption behavior (Song et al. 2004), and the N–N bond scission has been found to exclusively occur at step sites (the so-called B5 sites) on the Ru(001) surface (Dahl et al. 1999).

There are many relevant substrates for nanoparticle studies but in this particular study we have chosen HOPG because it is rather inert and electrically conductive. If the HOPG is freshly cleaved, it will expose large atomically flat terraces where the interaction with the nanoparticles is very weak, enabling studies of the properties of almost undisturbed nanoparticles (Yim et al. 2007; Zhang et al. 2007, 2008; Kadossov et al. 2008). It is also possible to intentionally create nucleation sites by ion bombardment of the HOPG (Kibsgaard et al. 2006; Rohmer et al. 2007; Yao et al. 2008) and a subsequent oxidation procedure can create nanopits in the surface (Song et al. 2004; Hinnemann et al. 2005) mimicking an activated carbon support in industrial catalysis (Rodriguez-reinoso 1998). In this study, we create nucleation sites on the surface by Ar^+ bombardment before nanoparticle deposition, and subsequently take advantage of the flatness of the HOPG to perform STM investigations.

The nanoparticles used in this study are produced using a magnetron-sputter gas-aggregation source. This type of source has been used for a wide range of applications (Granqvist and Buhrman 1976; Haberland et al. 1992; Binns 2001; Klipp et al. 2001; Pratontep et al. 2005), where primarily small clusters of less than a few hundred atoms have been investigated, but larger nanoparticles can also be produced with this type of source. The size range of the nanoparticles studied here is in the order of 2–15 nm, i.e., containing approximately 300–130,000 atoms, sizes well-suited for catalytic studies.

The morphology of the ruthenium nanoparticles has been investigated using a combination of scanning electron microscopy (SEM), scanning tunneling microscopy (STM), and transmission electron microscopy

(TEM). While the STM is prone to overestimating the nanoparticle diameter due to tip-convolution effects, it can provide an extremely accurate and reliable measure of the particle height (Hovel and Barke 2006). This complements data on the lateral dimensions of the particle obtained by TEM. By combining SEM, STM, and TEM data of the same samples, a detailed insight into the morphology of the nanoparticles can be obtained.

Experimental

Experiments were performed in a multichamber UHV system (Omicron Multiscan Lab) with a base pressure in the low 10^{-11} mbar region. The system consists of three separate chambers; an analysis chamber, a preparation chamber, and the nanoparticle source.

In the analysis chamber, the samples are analyzed using a combination of STM and SEM. The STM is an Omicron variable temperature microscope able to operate in a temperature interval from 70 to 650 K. The images reported here are obtained in constant current mode using a current of 100–700 pA and applying a gap voltage of 0.1–0.4 V. It was found that the measured particle height does not change substantially when changing the tunnel parameters in this range. In order to keep the noise level low and to avoid tip crashes due to slow feedback response, the scan speed was set to 0.5–1 Hz resulting in a scan time of approximately 10–20 min per image. The STM was calibrated using the well known atomic arrangement of the (7×7) reconstruction of Si(111) (Dujardin et al. 1996). The images were analyzed using the scanning probe image analysis software SPIP where the grain analysis tool was used to determine the mean height of the nanoparticles. The SEM is based around a Gemini column (Zeiss Supra 55VP) and operates at 1–20 kV with a working distance of 8 mm, resulting in a lateral resolution of approximately 3 nm. The SEM/STM information is supplemented with measurements using a Technai T20 200 kV TEM. The surface composition is studied with Auger electron spectroscopy (AES) using the electrons from the SEM and an Omicron NanoSAM hemispherical energy analyzer. The analyzer is also used to perform ion scattering spectroscopy (ISS) using an Omicron ISE 100 fine focus ion gun to produce He$^+$ ions.

The second chamber is used for sample preparation, where the sample can be Ar$^+$ sputtered using an Omicron ISE 10 ion gun and heated using a pyrolytic boron nitride (PBN) heater mounted on the backside of the sample. After the sample has been prepared, the nanoparticles from the gas-aggregation source can be deposited onto the sample while it remains in the preparation chamber.

The third main component of the system is the nanoparticle source from Mantis Deposition Ltd. The setup is illustrated in Fig. 1. The metal nanoparticles are formed by gas-phase condensation from a flux of ruthenium atoms, which are sputtered from a 99.99% purity ruthenium target. The flux of ruthenium atoms is provided by a magnetron sputtering head (c), located inside a liquid nitrogen cooled enclosure (d). Argon gas is used to provide the plasma at the magnetron sputtering head. It also facilitates the condensation of Ru clusters and their subsequent growth into nanoparticles. Helium gas may also be introduced into the aggregation zone to improve thermalization to obtain smaller particle sizes. The initial step in cluster formation has been suggested by Haberland et al. to involve a three body collision between two hot metal atoms and a cold argon atom (see Haberland et al. 1992 for further details). As the small clusters travel through the aggregation zone, they continue to grow by the sticking of additional Ru atoms to the cluster or by cluster–cluster collisions. By controlling key parameters, such as the sputtering power, aggregation distance, and the argon and helium flows, it is possible to control the residence time of the particles inside the aggregation zone and thereby tune the size of the nanoparticles exiting the nanoparticle source. For instance, an increased gas flow will decrease the residence time in the aggregation zone leading to smaller particles. After the particles are formed, they pass through two skimmers (e), reducing the local pressure from approximately $1–10^{-3}$ mbar (at an argon flow of 100 mL/min). The pressure difference gives rise to a supersonic expansion and further cooling of the nanoparticle beam. The nanoparticles enter the quadrupole mass filter (f), where the charged nanoparticles can be filtered according to their mass-to-charge ratio. According to Haberland et al. approximately 30–80% of nanoparticles exiting the aggregation zone carry a charge (Haberland et al. 1992). The mass selected particle production can be monitored by a quartz crystal
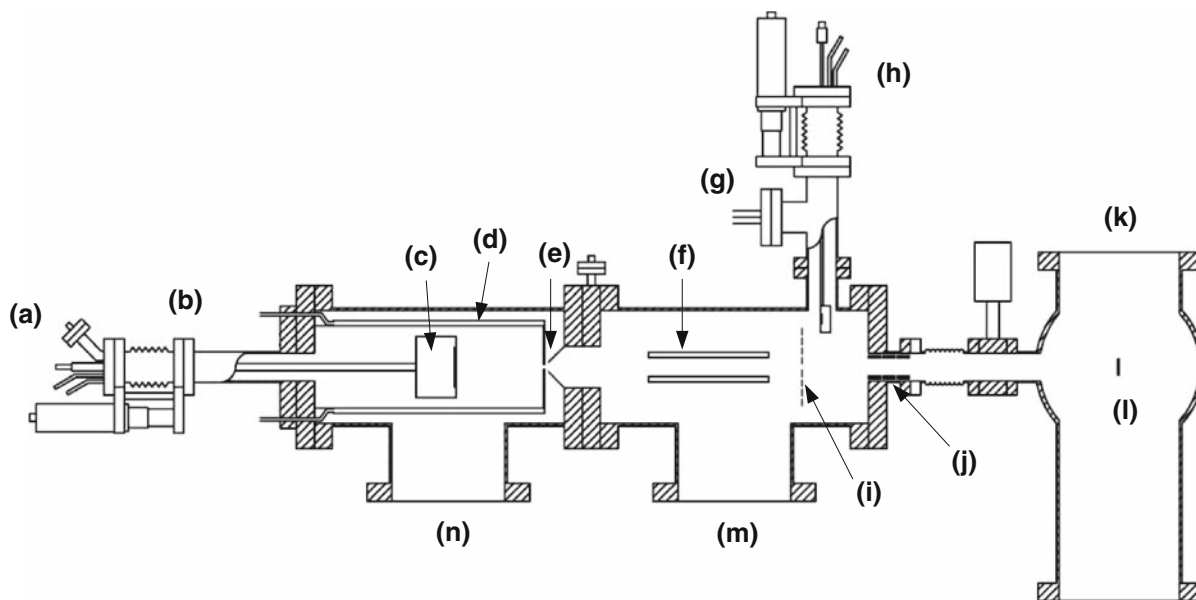
Fig. 1 Schematic of the cluster source. The gas inlet and power feedthrough to the magnetron sputtering head are seen to the left (**a**). The gas-aggregation distance can be altered using the linear translator (**b**). The magnetron sputtering head (**c**) is surrounded by a liquid nitrogen cooled enclosure (**d**). The nanoparticles pass through a 3 mm skimmer and a 6 mm conical aperture (**e**) and are then passed into the quadrupole mass filter (QMF) (**f**). The pressure is monitored using an ion-gauge (**g**). The nanoparticle production can be measured using a QCM (**h**) or a biased current plate (**i**). The nanoparticles are focused using an einzel lens (**j**) before entering the preparation chamber (**k**) and deposited onto the sample (**l**). The gas-aggregation source is pumped using 230 l/s (**m**) and 450 l/s (**n**) turbo molecular pumps

microbalance (QCM) (h) or on a biased current plate (i). A set of einzel lenses (j) are used to focus the nanoparticles onto the sample (l). The particles are soft-landed ($E_{kin} \leq 0.1$ eV/atom) onto the support surface (Moseler et al. 2002) by applying +36 V to the sample. By doing so, the nanoparticles are not deformed upon impact with the substrate which is known to occur at much larger biases (Carroll et al. 1998). A fraction of the produced nanoparticles are not charged and cannot be filtered by the quadrupole. This fraction will, however, decrease significantly going through the mass filter and the einzel lens due to focusing of the charged particles. Blind experiments show that the fraction (the relative coverage) of the neutrals when the sample is positioned in direct line-of-sight of the source is less than 1%. At times, very large particles (> 50 nm) are observed, which are believed to be neutral nanoparticles that have reached the sample.

In order to avoid contamination of the nanoparticles, the source must be baked at 150 °C under vacuum for approximately 24 h prior to use, leading to a base pressure of approximately 5×10^{-10} Torr.

The helium and argon gases are of N60 purity and are further purified by passing them over an iron catalyst, which adsorbs most of the remaining contaminants, such as CO, CO_2, and H_2O. The iron catalysts are activated by baking them in a stream of hydrogen at 3 bar and 450 °C for several days.

The quadrupole rods are paired, with each pair sitting diagonally opposite from one another. In order to select masses, a DC voltage (V) and an AC voltage (U) with frequency denoted f are applied to the four quadrupole rods, with each pair having an opposite polarization. The mass filtered by the quadrupole is determined by f, U, and the spacing of the rods, while the resolution is determined by the ratio between U and V. The optimum resolution is achieved for a U/V ratio of approximately 0.1678 (Paul et al. 1958). However, at this high resolution only very small particle currents, less than 1 pA, are obtained at the sample. Therefore, as a compromise a theoretical resolution of approximately 6% in the particle diameter (U/V = 0.12) is chosen, where currents of 10–100 pA are achieved. The quadrupole selects a given mass according to the settings on the four rods

of the mass filter. From this mass, we calculate the corresponding diameter of a spherical nanoparticle, assuming it has the density of the bulk material. This diameter, denoted D_{MF} where MF stands for "mass filter" is defined as:

$$D_{MF} = \sqrt[3]{\frac{6 \cdot m}{\pi \cdot \rho}} \qquad (1)$$

where m is the mass of the selected nanoparticle and ρ is the density of the bulk material.

The ruthenium nanoparticles were deposited onto HOPG for STM studies in UHV and onto lacey carbon grids for TEM analysis. The HOPG substrates used (SPI-1, 7 mm × 7 mm × 0.5 mm) were mounted in a sample holder incorporating a PBN heater to provide radiative heating to the back side of the substrate. A 0.25-mm W–5 at% Re/W–26 at% Re thermocouple was pressed against the front side of the HOPG substrate and the sample temperature could be regulated through a PID controller (Eurotherm 2408). The HOPG was cleaved in air before loading into the UHV system, where it was outgassed for several hours at ~650 °C. The surface was etched with 500 eV Ar^+ ions for 15 min with a current of approximately 0.1 μA/cm^2, followed by annealing at ~650 °C for 15 min to degas the surface of implanted argon. The sputtering step was performed to create a highly defected surface where the pre-formed particles could stick to prevent sintering at elevated temperatures (Claeyssens et al. 2006).

Results

Production of ruthenium nanoparticles from the magnetron aggregation source

The aggregation source was optimized to produce ruthenium particles with D_{MF} values of 2–10 nm. A principal factor in determining the particle size was found to be the flow of argon through the aggregation zone. In Fig. 2a, spectra of the particle production for different Ar flows are measured with the sputtering power held constant at 37 W. The spectra are obtained by varying the frequency of the AC voltage applied to the quadrupole rods, while keeping the amplitudes of both the AC and DC voltages constant. As shown in Fig. 2a, it is possible to create

nanoparticles in the size range of 4–10 nm, solely by controlling the Ar flow through the source. As expected, the particle size increases as the flow is decreased. When very large particles are produced, the particle current is seen to drop significantly. However, if the current is integrated over the mass range, the ruthenium output is in fact almost constant.

Smaller nanoparticles can be produced by introducing helium into the aggregation zone. This is seen in Fig. 2b where the source has been optimized for small nanoparticles. Here, the aggregation distance has been decreased by 37 mm by moving the magnetron forward into the aggregation zone while keeping all other parameters unaltered. With only the Ar flow present, it is seen that almost no nanoparticles are formed under these conditions. As the helium flow is introduced, the production of nanoparticles is seen to increase, and increasing the helium flow results in a further decrease in the size of the nanoparticles. It is clearly seen in Fig. 2b that certain sizes are favored over others. Particles with D_{MF} values of 1.75, 2.5, and 3.0 nm have a higher probability of formation than other sizes. The origin of these preferred sizes is not clear at this stage.

The position and shape of the spectra seen in Fig. 2 are reproducible, even after air exposure, followed by pump down and bakeout. Without the bakeout, the nanoparticle production is unstable and changes with time. The bakeout is thus an essential part of creating ruthenium nanoparticles reproducibly from the gas-aggregation source.

Surface analysis of ruthenium nanoparticles

The purity of the nanoparticles was checked by AES. A measurement of a HOPG sample completely covered by Ru nanoparticles with a $D_{MF} = 8$ nm is shown in Fig. 3a. The characteristic ruthenium lines at 205, 235, and 277 eV, are clearly observed. The carbon line at 275 eV overlaps with ruthenium and it is thus very difficult to distinguish from ruthenium. Furthermore, it is unfortunately not possible to distinguish whether or not part of the carbon signal could originate from carbon situated on the particles or if it only originates from the substrate. No other elements could be detected by AES.

The surface cleanliness was also analyzed using ISS. An example of an ISS spectrum of particles with $D_{MF} = 7$ nm is presented in Fig. 3b. The dominant

Fig. 2 Particle production
(ion current) as a function
of D_{MF}, derived from the
mass filter settings. **a** The
particle production for a
range of argon flows
without the presence of
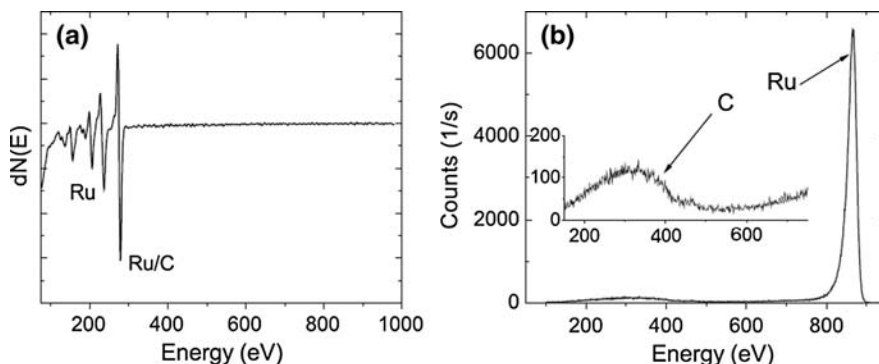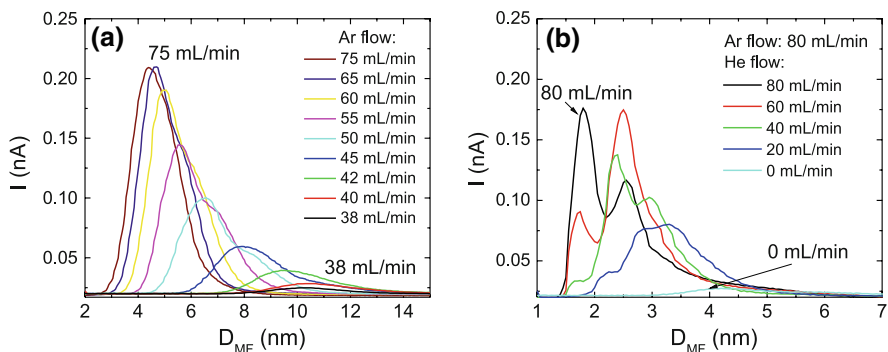helium. **b** Smaller particles
can be produced by
introducing helium

Fig. 3 Surface sensitive spectroscopy of ruthenium nanoparticles on HOPG. **a** an AES spectrum of a complete layer of ruthenium nanoparticles deposited onto HOPG is shown. **b** an ISS spectrum of ruthenium nanoparticles deposited on HOPG

is shown with the Ru peak indicated. In the inset of **b**, the low energy regime is enlarged which reveals the signal from carbon. No contamination could be detected with AES or ISS

peak at 865 eV is from ruthenium. An enlargement of
the low energy part of the spectra is shown in the
inset, where the broad feature at 250–350 eV is
believed to originate from the carbon substrate.
Carbon has a very high neutralization probability,
and it is very difficult to detect in ISS (Luna et al.
2008). No other elements could be detected by ISS.

Model of ruthenium nanoparticles

The expected morphology of an equilibrated hexag-
onal close packed ruthenium nanoparticle is the
truncated hexagonal bipyramid, found for instance by
Gavnholt and Schiøtz (2008). In Fig. 4, a Wulff
construction of a nanoparticle consisting of 83,478
atoms is displayed. The morphology of the particle is
determined from the surface energies of the various
facets (Gavnholt 2009). For ruthenium, the (001),
(100), and (011) facets have the lowest energies and
thus dominate the surface area of the nanoparticle.

By observing the same particle from different
angles, see Fig. 4, the two-dimensional projection of
the particle will vary slightly. The projection of the
nanoparticle in Fig. 4a is clearly hexagonal, whereas
the projection appears octagonal in Fig. 4b and
almost spherical in Fig. 4c. When the particles are
imaged by SEM and TEM, it is the two-dimensional
projection that is seen and since the particle appears
slightly different depending on its orientation, two-
dimensional projections of identical particles will
appear differently. Consequently, the projection of
the particle seen in Fig. 4 can be interpreted to have
diameters in the range of 11.9–12.5 nm depending on
which angle it is observed from. Furthermore, the
number of atoms in the particle seen in Fig. 4 is
optimized to achieve a well-terminated Wulff con-
struction. If atoms are added to the particle or the
particle has a morphology slightly different from the
equilibrium state, the two-dimensional projections
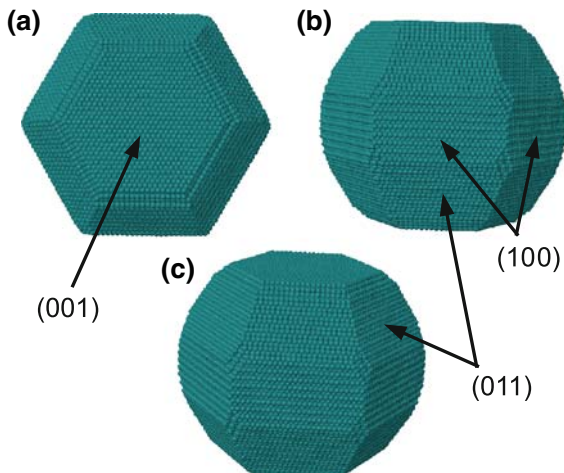will become even more diverse.

Fig. 4 Different views of a Wulff construction of a particle consisting of 83,478 atoms corresponding to $D_{MF} = 12.9$ nm according to Eq. 1. The dominating surfaces are the (001), (100), and (011) facets since these facets have the lowest surface energies. Due to the different surface energies of the facets, the observed width (the diameter) of the particle will depend on which projection the particle exhibits in the TEM

The size of ruthenium nanoparticles

SEM

The nanoparticle ensembles were first imaged with SEM under UHV to obtain a global overview of the coverage and the spatial distribution of the particles on the surface. An example is shown in Fig. 5 which shows a SEM image of particles with $D_{MF} = 9$ nm that have been soft-landed onto sputtered HOPG at room temperature. The nanoparticles are distributed across the surface and there are no signs of sintering or step decoration. It can, therefore, be concluded that when the particles arrive on the surface they are immediately pinned by defects and do not diffuse around the surface. SEM analysis was performed on
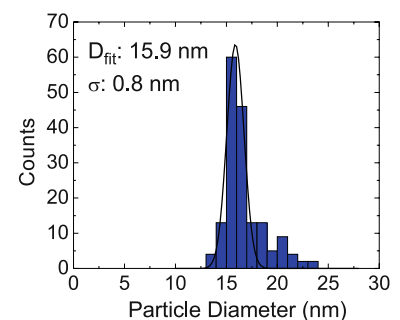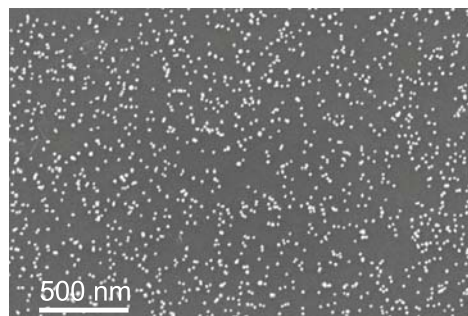
different samples with different particle sizes and showed that the nanoparticles were for the most part isolated from one another on the surface, thereby minimizing any effects that may arise from particle–particle interactions. A small fraction of the particles were, however, observed in close proximity to one another, which we attribute to the random deposition process. The mean diameter of the particles as measured by SEM is 15.9 ± 0.8 nm. The particles are thus very monodisperse, but they appear to be larger than the mass from the quadrupole mass filter would suggest. The SEM resolution of 3 nm may cause smearing out of the particles, leading to a shift up in the measured particle size.

STM

Using the STM, it is possible to obtain three dimensional information of the particle morphology. Examples of nanoparticles imaged with the STM are shown in Fig. 6 along with the corresponding height distributions. Fig. 6a shows an STM image of ruthenium nanoparticles with $D_{MF} = 2.3$ nm. The image shows no sign of sintering of the nanoparticles. The height of the particles (2.4 ± 0.5 nm) extracted from the height distribution shown to the right in Fig. 6a agrees well with the size (D_{MF}) extracted from Eq. 1. In Fig. 6b, a STM image of nanoparticles with $D_{MF} = 7$ nm is presented. The particles are seen to be monodisperse, with an average height of 9.9 ± 1.2 nm, which is somewhat higher than the corresponding D_{MF} value. In Fig. 7, the height measured by STM for a range of particle sizes is presented. The spread in the measured particle height is influenced by the root-mean-square roughness of the sputtered HOPG which has been found to be approximately 1 nm. The narrow spread seen for the nanoparticle heights are thus very satisfying. The height is seen to agree well with the

Fig. 5 SEM image (5 kV, 1 nA) of ruthenium nanoparticles with $D_{MF} = 9$ nm with the size distribution shown to the right

Fig. 6 STM images of ruthenium nanoparticles with $D_{MF} = 2.3$ nm (**a**) and 7 nm particles (**b**). To the right of each image, the height distribution is shown along with the average height and standard deviation
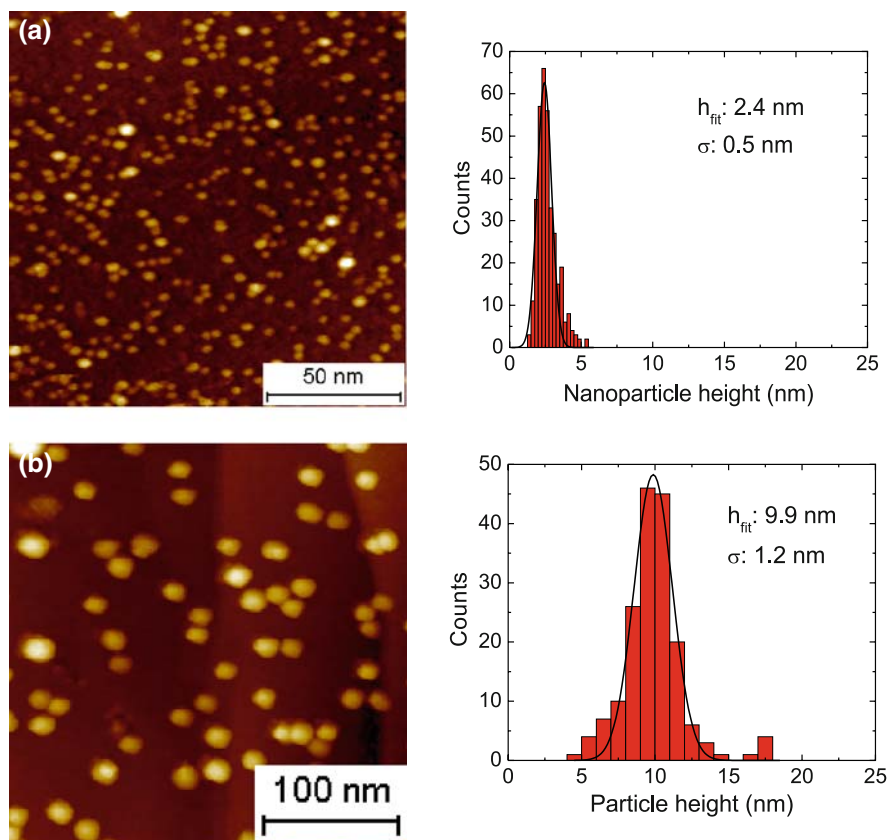
diameter of the spherical particle (D_{MF}) at the lower sizes. For sizes larger than 6 nm, however, the measured particle height is seen to deviate significantly from D_{MF}. For instance at $D_{MF} = 9$ nm, the measured particle height is 15.6 ± 1.5 nm.

As the particle is imaged with an STM tip, the final image of the particle will be a convolution of the tip and the particle and since the tip has a finite size, the nanoparticle diameter may appear larger than it actually is. This effect will be more apparent when the nanoparticle diameter becomes similar to or smaller than the radius of curvature of the STM tip which is expected to be not better than 5–10 nm (Nakamura et al. 1999; Guise et al. 2002). It is thus hard to obtain an accurate measurement of the particle diameter using STM, but very accurate measurements of the particle height can, however, be obtained with STM.

TEM

In order to investigate the diameter with a higher resolution than the in situ SEM and to avoid the

tip-convolution effects in STM mentioned above, the particles are imaged with TEM. Here, the diameter of the two-dimensional projection is easily obtained, although no information about the height of the nanoparticles is provided. TEM images of two different nanoparticle sizes with $D_{MF} = 3$ and 7.5 nm are presented in Fig. 8a and b, respectively. In the size distributions in Fig. 8 (shown to the right of each image), it is seen that the nanoparticles with $D_{MF} = 3$ nm agree very well with the spherical model whereas the particles with $D_{MF} = 7.5$ nm are in fact ~ 10.8 nm. The spread in the diameter is 0.5 nm ($\pm 18\%$) and 0.8 nm ($\pm 7\%$) for the 3 and 7.5 nm particles, respectively. The expected spread in diameter is approximately 6% for the quadrupole settings used. However, as mentioned previously, the particle size distribution is expected to be slightly smeared out due to the different cross sections of the particles. The spread in particle size is thus very satisfying taking this into account.

The diameters obtained from TEM are plotted in Fig. 7 along with the STM data. It is seen, that the diameter obtained with TEM and the height measured
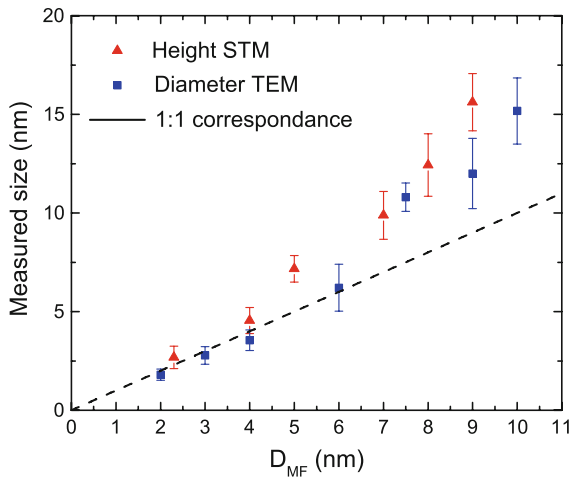
Fig. 7 The measured nanoparticle size versus D_{MF}. The *error bars* represent the standard deviation from the Gaussian fits. The *dashed line* displays the 1:1 correspondence between the measured height/diameter and D_{MF} and is shown to guide the eye. Nanoparticles are seen to have approximately the same height and diameter for all mass selections. At larger sizes, a deviation from D_{MF} is observed

by STM agree well with the size extracted from the spherical model for $D_{MF} < 6$ nm. For larger particles, the measured diameter is seen to deviate by several nanometers from the 1:1 correlation.

The height of the nanoparticles measured by STM is seen to follow the diameter obtained from TEM very well in the entire size range investigated. The particles are thus uniform in all directions with an aspect ratio of approximately one, even though the size deviates from the size extracted from the quadrupole settings. Since the deposited particles follow the same trend they are believed to retain their shape as they are deposited. This confirms that the particles are in fact soft-landed onto the surface and do not change shape significantly upon impact.

Particles with $D_{MF} = 10$ nm are seen to have an actual size of approximately 15 nm. This difference corresponds to a shift in particle mass from approximately 38,000 atoms to 130,000 atoms. The mass of the particles is, therefore, more than three times higher than expected. The size resolutions of these

Fig. 8 TEM images of ruthenium nanoparticles with $D_{MF} = 3$ nm (**a**) and 7.5 nm (**b**). To the right of each image, the size distribution is shown along with the average diameter and the standard deviation. TEM diameters for several sizes are included in Fig. 7
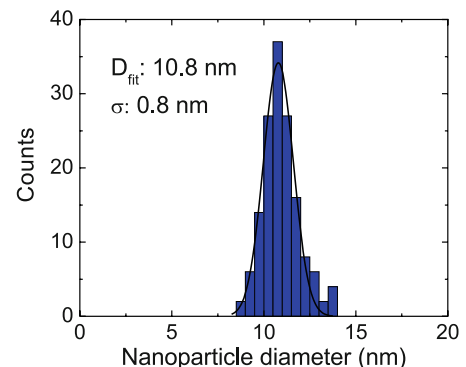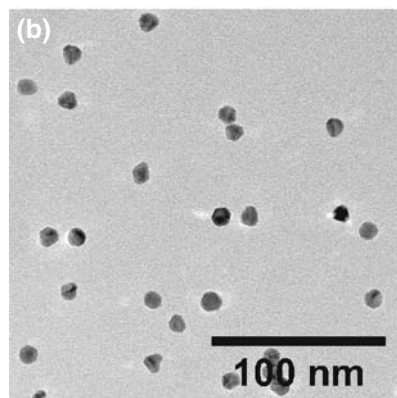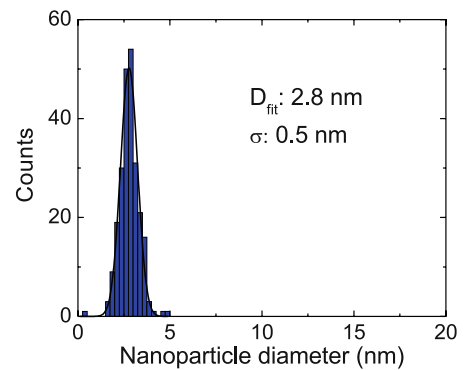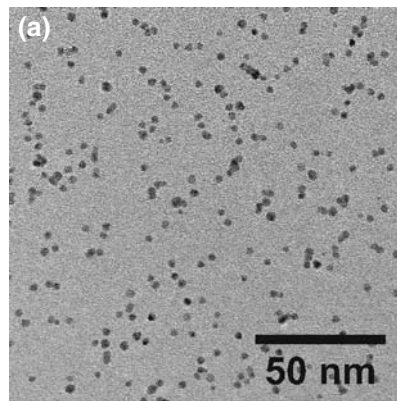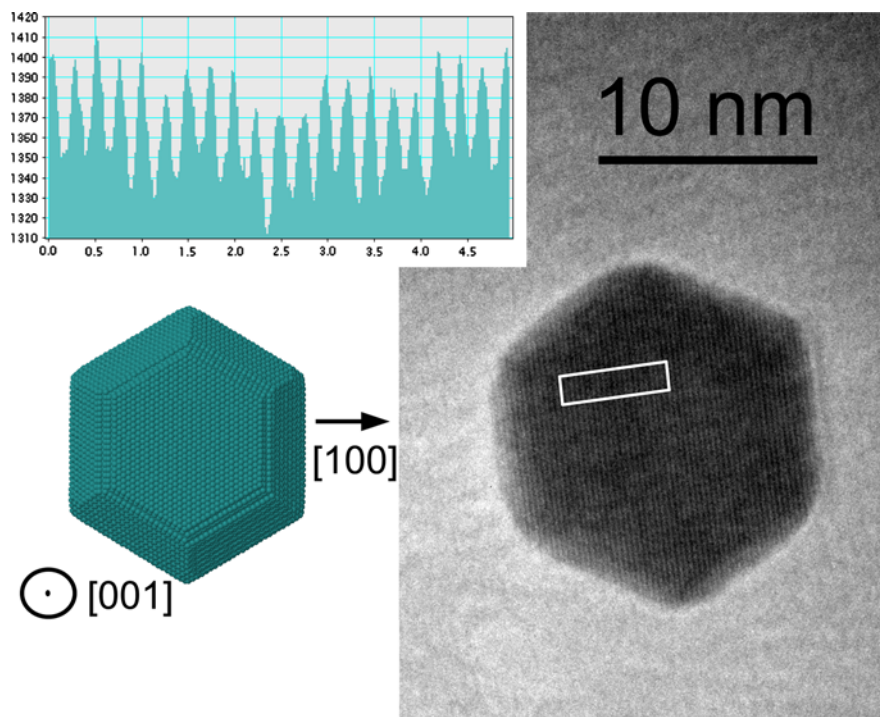
particles are in all cases within the expected resolution and the actual selected masses are just shifted toward larger sizes. It is not obvious at this point why the mass filter is presumably not accurate on an absolute scale at the highest masses. However, the measurements presented in Fig. 7 can be used directly for calibration of the mass filter. Consequently, a reproducible particle production with a narrow size distribution is achievable for nanoparticles in the diameter range of 2–15 nm. This range is ideal for studies of the catalytic properties of Ru nanoparticles. For example, Gavnholt and Schiøtz have predicted an optimal Ru nanoparticle diameter of 3 nm for ammonia synthesis (Gavnholt and Schiøtz 2008).

Nanoparticle morphology

The TEM can be used to investigate the crystalline structure of the ruthenium nanoparticles as well as their morphology. Often, it is possible to detect lattice fringes from the particles deposited on the lacey carbon surface.

The particle measured by TEM shown in Fig. 9 has a diameter of approximately 15 nm and the lattice fringes are found to be approximately 0.24 nm apart.

Comparing the nanoparticle to the Wulff constructed model, it is seen that the projection would agree with a nanoparticle with the (001) crystallographic plane comprising the top facet and the [100] direction pointing to the right as illustrated in Fig. 9. The (100) interplanar distance is 0.23 nm which agrees well with the lattice fringes seen in the figure.

Since ruthenium binds oxygen strongly (Madey et al. 1975) the surface of the particles may be oxidized during transfer to the TEM. The lattice fringes in Fig. 9, however, suggest that the bulk part of the particle remains metallic. This agrees well with the study by Jones et al. who found that ruthenium nanoparticles in the size range of 2–4 nm created ex-situ are not visible in the TEM due to the particles being bulk oxidized. They found that the particles had to be reduced in hydrogen to become visible in TEM (Jones et al. 2008). Consequently, our nanoparticles imaged by TEM are believed to have the same morphology and crystalline structure as the particles imaged with in situ STM.

In Fig. 10, various morphologies of 6 nm particles are shown. The particles are seen mostly to exhibit hexagonal symmetry. The specific shape is, however, not the same for all the particles. The shape varies from perfect hexagonal in Fig. 10a, through a

Fig. 9 TEM of a ruthenium nanoparticle with $D_{MF} = 10$ nm where lattice fringes are clearly seen. A line profile within the indicated area on the TEM image is shown in the inset, where the average periodicity is found to be 0.24 nm which fits well with the (100) interplane distance of 0.23 nm. Also shown is a possible model of a nanoparticle with the [001] direction pointing normal to the page

Fig. 10 Examples of high resolution TEM images of $D_{MF} = 6$ nm ruthenium nanoparticles (**a–d**). The morphology of the particles is mostly of hexagonal symmetry, with a range of different polymorphs
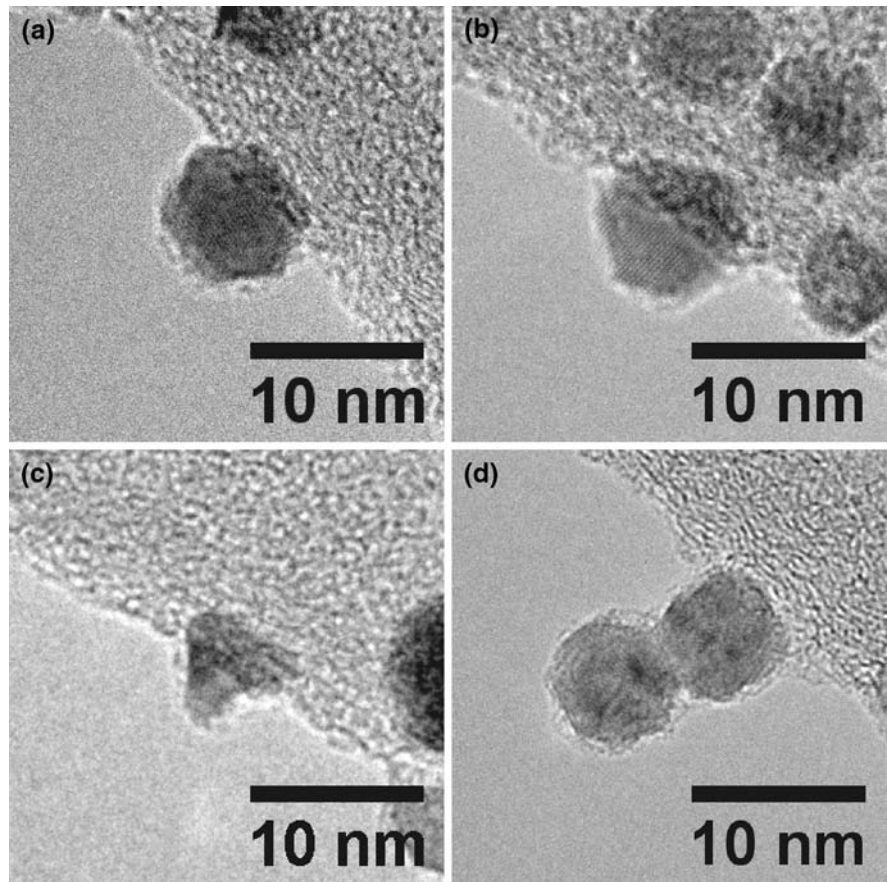
truncated hexagonal in Fig. 10b, to an almost triangular particle in Fig. 10c. The two particles on top of each other in Fig. 10d do not appear to have hexagonal symmetry. This, however, does not exclude the possibility that the particles are truncated hexagonal bipyramids. The two-dimensional projection of the particle seen in Fig. 4c is, e.g., similar to the shape seen in Fig. 10d. In general, nanoparticles smaller than approximately 6 nm appear to have well-defined surfaces. The particles are primarily found to have hexagonal symmetry with a range of different polymorphs present.

As the size is increased further to the maximum possible size of 15 nm, the diversity of morphologies becomes gradually larger. For the largest particle sizes, hexagonal particles are at times observed as observed in Fig. 9. However, the majority of the largest particles have rough surfaces (see Fig. 11a, b) and the morphology does not display the thermodynamic equilibrium shape seen in Fig. 4. Several examples of multiple particle morphologies are

observed for particles above a measured diameter of approximately 10 nm. The particle displayed in Fig. 11c appears to consist of smaller particles which have agglomerated inside the nanoparticle source. The multiple particle appears to have the correct size compared to the predominant particle shape and it is thus believed that this type of particle is formed inside the cluster source rather than by sintering on the surface. These agglomerates of multiple smaller particles have been observed for all measured particle sizes above approximately 10 nm, but the fraction of these particles present on the surface is less than 1% of the total deposit and, therefore, does not contribute significantly to the size distribution.

Discussion

The height determined by STM and the diameter extracted from TEM agree well with D_{MF} up to a value of approximately 6 nm. For larger nanoparticles, the
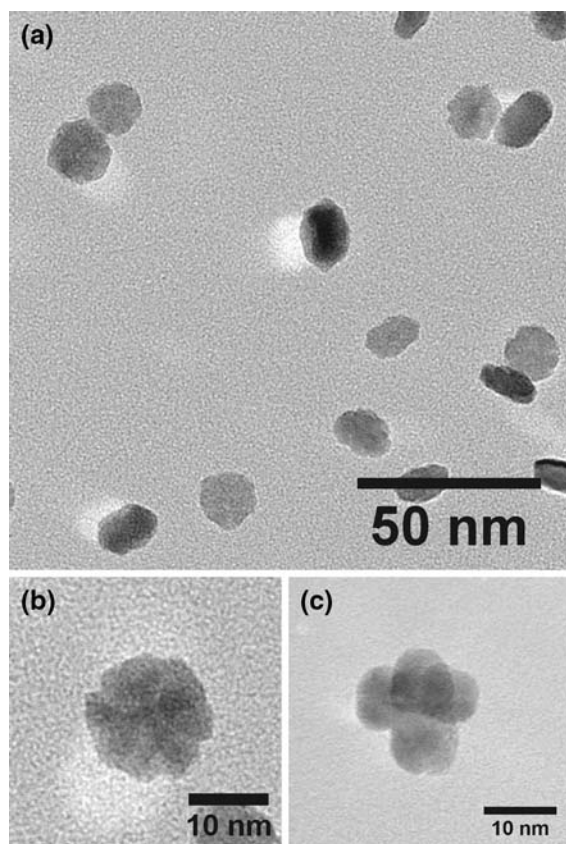
Fig. 11 Examples of different morphologies of $D_{MF} = 15$ nm ruthenium nanoparticles (**a–c**). The diversity of the nanoparticle morphology is obvious. Several particles are very far from equilibrium exhibiting sharp dents in the side of the particles (**b**). A particle which appears to consist of four smaller particles is also observed (**c**)

diameter and height are seen to be increasingly larger than D_{MF}. The reason for this is not clear at this stage. Small deviations could be explained by the geometry not being correctly incorporated in D_{MF}. Perhaps, these very high masses (a nanoparticle of 6–7 nm contains $\sim 10,000$ atoms corresponding to roughly one million amu) may cause a non-ideal expansion from the aggregation zone into the mass filter. Additionally, there might also be a break-down of some of the basic assumptions for this type of mass filter, which is typically used for much smaller masses. Such matters are, however, beyond the scope of the present study. The larger particles might also exit the cluster source with multiple charges. If the largest particles were charged by three electrons instead of one, the size would in fact fit well. However, if multi-charged particles were present, different peaks should be visible

in the particle production measurements. Since this is never seen, the number of multi-charged particles is believed to be insignificant. Despite the unexplained behavior at higher masses, our mass filter works well and can be used to produce nanoparticles with a specific diameter by calibrating according to the data presented in Fig. 7.

The high resolution TEM images of the nanoparticles in Figs. 10 and 11 showed that a number of different particle shapes are present on the surface. Particularly, the largest particles have very diverse particle morphologies. It is believed that the morphology of all these particles are determined in the gas-aggregation source. In this type of source, the particles are created by ruthenium atoms while transitioning from a hot plasma in the vicinity of the sputter target to a cold inert gas environment in the aggregation zone. This rapid quenching of the nanoparticles could of course lead to numerous non-equilibrium shapes being adopted. The smaller nanoparticles with a diameter less than 6 nm also have slightly different morphologies, but the diversity is not as evident as is observed for the larger particles. The shape of the smaller particles appears to be closer to the equilibrium shape.

The particles are intended for investigation of the structure dependency of catalytic reactions. Since the diversity of the particles become increasingly larger as the particle size is increased above 6 nm, it is difficult to correlate the catalytic properties of the large particles to the morphology. It might be possible to anneal the particles such that they reach the equilibrium shape. This annealing should ideally take place in the gas phase before deposition to prevent any sintering of the particles due to the annealing, but alternatively it could be carried out after deposition. While the larger particles are not ideal for correlation studies, they may actually be very active catalysts due to the rather rough surface and thus large quantity of low-coordinated sites. It would be very interesting to compare the catalytic activity of these non-equilibrium shaped model catalysts to commercially available Ru catalysts.

Conclusions

- By varying nanoparticle source parameters such as argon flow and aggregation distance, we are

able to produce size-selected ruthenium nanoparticles in the range from 2 to 15 nm.

- The formation of 1.75, 2.5, and 3.0 nm diameter nanoparticles is favored over other sizes at the lower end of the size range studied. For larger sizes, there is no evidence of sizes more favorable than others.

- The size distributions show a spread of approximately ±10% when deposited on either HOPG surfaces or lacey carbon films.

- Small nanoparticles are seen in the TEM to be crystalline, with various hexagonal symmetries.

- Larger nanoparticles are also crystalline as demonstrated by the fact that we observe lattice fringes consistent with metallic Ru in TEM images of these particles. However, they exhibit a large variety of shapes, including what are clearly agglomerates of smaller nanoparticles and particles with very rough surfaces. It is believed that the particle morphology is determined in the gas-aggregation source.

- The smaller particles are well-defined in shape and size and are, therefore, very suitable as model catalysts. The larger particles are on the other hand less well-defined and are thus not as ideal for correlation studies. They may, however, be quite active catalysts.

References

Andersson MP, Abild-Pedersen F, Remediakis IN, Bligaard T, Jones G, Engbæk J, Lytken O, Horch S, Nielsen JH, Sehested J, Rostrup-Nielsen JR, Nørskov JK, Chorkendorff I (2008) Structure sensitivity of the methanation reaction: H_2-induced CO dissociation on nickel surfaces. J Catal 255:6–19

Bielawa H, Hinrichsen O, Birkner A, Muhler M (2001) The ammonia-synthesis catalyst of the next generation: barium-promoted oxide-supported ruthenium. Angew Chem Int Ed 40:1061–1063

Binns C (2001) Nanoclusters deposited on surfaces. Surf Sci Rep 44:1–49

Carroll SJ, Hall SG, Palmer RE, Smith R (1998) Energetic impact of size-selected metal cluster ions on graphite. Phys Rev Lett 81:3715–3718

Claeyssens F, Pratontep S, Xirouchaki C, Palmer RE (2006) Immobilization of large size-selected silver clusters on graphite. Nanotechnology 17:805–807

Croy JR, Mostafa S, Liu J, Sohn Y-H, Cuenya BR (2007) Size dependent study of MeOH decomposition over size-selected Pt nanoparticles synthesized via micelle encapsulation. Catal Lett 118:1–7

Dahl S, Logadottir A, Egeberg RC, Larsen JH, Chorkendorff I, Törnqvist E, Nørskov JK (1999) Role of steps in N_2 activation on Ru(0001). Phys Rev Lett 83:1814–1817

den Breejen JP, Radstake PB, Bezemer GL, Bitter JH, Frøseth V, Holmen A, de Jong KP (2009) On the origin of the cobalt particle size effects in Fischer-Tropsch catalysis. J Am Chem Soc 131:7197–7203

Dujardin G, Mayne A, Comtet G, Hellner L, Jamet M, Le Goff E, Millet P (1996) New model of the initial stages of Si(111)-(7x7) oxidation. Phys Rev Lett 76:3782–3785

Frank M, Bäumer M (2000) From atoms to crystallites: adsorption on oxide-supported metal particles. Phys Chem Chem Phys 2:3723–3737

Gavnholt J (2009) The structure of individual nanoparticles and hot electron assisted chemistry at surfaces. Dissertation, Technical University of Denmark

Gavnholt J, Schiøtz J (2008) Structure and reactivity of ruthenium nanoparticles. Phys Rev B 77:035404-1-035404-10

Geng D, LuG (2007) Size effect of gold nanoparticles on the electrocatalytic oxidation of carbon monoxide in alkaline solution. J Nanopart Res 9:1145–1151

Granqvist CG, Buhrman RA (1976) Ultrafine metal particles. J Appl Phys 47:2200–2219

Grunwaldt J-D, Molenbroek AM, Topsøe N-Y, Topsøe H, Clausen BS (2000) In situ investigations of structural changes in Cu/ZnO catalysts. J Catal 194:452–460

Guise OL, Ahner JW, Jung MC, Goughnour PC, Yates JT (2002) Reproducible electrochemical etching of tungsten probe tips. Nano Lett 2:191–193

Haberland H, Karrais M, Mall M, Thurner Y (1992) Thin-films from energetic cluster impact—a feasibility study. J Vac Sci Technol A 10:3266–3271

Hammer B, Norskov JK (2000) Theoretical surface science and catalysis—Calculations and concepts. Adv Catal 45:71–129

Hansen PL, Wagner JB, Helveg S, Rostrup-Nielsen JR, Clausen BS, Topsøe H (2002) Atom-resolved imaging of dynamic shape changes in supported copper nanocrystals. Science 295:2053–2255

Haruta M, Yamada N, Kobayashi T, Iijima S (1989) Gold catalysts prepared by coprecipitation for low-temperature oxidation of hydrogen and of carbon-monoxide. J Catal 115:301–309

Hinnemann B, Moses PG, Bonde J, Jørgensen KP, Nielsen JH, Horch S, Chorkendorff I, Nørskov JK (2005) Biomimetic hydrogen evolution: MoS2 nanoparticles as catalyst for hydrogen evolution. J Am Chem Soc 127:5308–5309

Honkala K, Hellman A, Remediakis IN, Logadottir A, Carlsson A, Dahl S, Christensen CH, Nørskov JK (2005) Ammonia synthesis from first-principles calculations. Science 307:555–558

Hovel H, Barke I (2006) Morphology and electronic structure of gold clusters on graphite: Scanning-tunneling techniques and photoemission. Prog Surf Sci 81:53–111

Jacobsen CJH, Dahl S, Hansen PL, Törnqvist E, Jensen L, Topsøe H, Prip DV, Møenshaug PB, Chorkendorff I (2000) Structure sensitivity of supported ruthenium catalysts for ammonia synthesis. J Mol Catal A Chem 163:19–26

Janssens TVW, Clausen BS, Hvolbæk B, Falsig H, Christiansen CH, Bligaard T, Nørskov JK (2007) Insights into the reactivity of supported Au nanoparticles: combining theory and experiment. Top Catal 44:15–26

Jones G, Jakobsen JG, Shim SS, Kleis J, Andersson MP, Rossmeisl J, Abild-Pedersen F, Bligaard T, Helveg S, Hinnemann B, Rostrup-Nielsen JR, Chorkendorff I, Sehested J, Nørskov JK (2008) First principles calculations and experimental insight into methane steam reforming over transition metal catalysts. J Catal 259:147–160

Kadossov E, Funk S, Burghaus U (2008) CO adsorption of FeOx nanoclusters supported on HOPG—effect of oxide formation on catalytic activity. Catal Lett 120:179–183

Kibsgaard J, Lauritsen JV, Lægsgaard E, Clausen BS, Topsøe H, Besenbacher F (2006) Cluster-support interactions and morphology of MoS2 nanoclusters in a graphite-supported hydrotreating model catalyst. J Am Chem Soc 128: 13950–13958

King DL (1978) Fischer-Tropsch study of supported ruthenium catalysts. J Catal 51:386–397

Klipp B, Grass M, Müller J, Stolcic D, Lutz U, Ganteför G, Boneberg J, Leiderer P (2001) Deposition of mass-selected cluster ions using a pulsed arc cluster-ion source. Appl Phys A 73:547–554

Kung MC, Davis RJ, Kung HH (2007) Understanding Au-catalyzed low-temperature CO oxidation. J Phys Chem C 111:11767–11775

Landman U, Yoon B, Zhang C, Heiz U, Arenz M (2007) Factors in gold nanocatalysis: oxidation of CO in the non-scalable size regime. Top Catal 44:145–158

Luna NB, Bonetto FJ, Vidal RA, Goldberg EC, Ferrn J (2008) Low energy ion scattering in He/HOPG system. J Mol Catal A 281:237–240

Madey TE, Engelhardt HA, Menzel D (1975) Adsorption of oxygen and oxidation of CO on the ruthenium (001) surface. Surf Sci 48:304–328

Moseler M, Häkkinen H, Landman U (2002) Supported magnetic nanoclusters: soft landing of Pd clusters on a MgO surface. Phys Rev Lett 89:176103-1–176103-4

Nakamura Y, Mera Y, Maeda K (1999) A reproducible method to fabricate atomically sharp tips for scanning tunneling microscopy. Rev Sci Instrum 70:3373–3376

Nørskov JK, Bligaard T, Hvolbæk B, Abild-Pedersen F, Chorkendorff I, Christensen CH (2008) The nature of the active site in heterogeneous metal catalysis. Chem Soc Rev 37:2163–2171

Paul W, Reinhard HP, Vonzahn U (1958) Das elektrische massenfilter als massenspektrometer und isotopentrenner. Z für Phys 152:143–182

Pratontep S, Carroll SJ, Xirouchaki C, Streun M, Palmer RE (2005) Size-selected cluster beam source based on radio frequency magnetron plasma sputtering and gas condensation. Rev Sci Instrum 76:1–8

Rodriguez-reinoso F (1998) The role of carbon materials in heterogeneous catalysis. Carbon 36:159–175

Rohmer M, Ghaleh F, Aeschlimann M, Bauer M, Hövel H (2007) Mapping the femtosecond dynamics of supported clusters with nanometer resolution. Eur Phys J D 45:491–499

Sanchez A, Abbet S, Heiz U, Scheider WD, Häkkinen H, Barnett RN, Landman U (1999) When gold is not noble: nanoscale gold catalysts. J Phys Chem A 103:9573–9578

Shincho E, Egawa C, Naito S, Tamaru K (1985) The behavior of CO adsorbed on Ru (1, 1, 10) and Ru(001)—the dissociation of CO at the step sites of the Ru(1, 1, 10) surface. Surf Sci 149:1–16

Silvestre-Albero J, Rupprechter G, Freund H-J (2006) Atmospheric pressure studies of selective 1, 3-butadiene hydrogenation on well-defined Pd/Al2O3/NiAl(110) model catalysts: effect of Pd particle size. J Catal 240:58–65

Song Z, Cai T, Hanson JC, Rodriguez JA, Hrbek J (2004) Ru nanoclusters prepared by Ru3(CO)12 deposition on Au(111). J Am Chem Soc 126:8576–8584

Tian N, Zhou Z-Y, Sun S-G, Ding Y, Wang ZL (2007) Synthesis of tetrahexahedral platinum nanocrystals with high-index facets and high electro-oxidation activity. Science 316:732–735

Valden M, Lai X, Goodman DW (1998) Onset of catalytic activity of gold clusters on titania with the appearance of nonmetallic properties. Science 281:1647–1650

Wörz AS, Judai K, Abbet S, Heiz U (2003) Cluster size-dependent mechanisms of the CO + NO reaction on small Pd-n (n ≤ 30) clusters on oxide surfaces. J Am Chem Soc 125:7964–7970

Yao Y, Fu Q, Zhang Z, Zhang H, Ma T, Tan D, Bao X (2008) Structure control of Pt–Sn bimetallic catalyst supported on highly oriented pyrolytic graphite (HOPG). Appl Surf Sci 254:3808–3812

Yim W-L, Nowitzki T, Necke M, Schnars H, Nickut P, Biener J, Biener MM, Zielasek V, Al-Shamery K, Klüver T, Bäumer M (2007) Universal phenomena of CO adsorption on gold surfaces with low-coordinated sites. J Phys Chem C 111:445–451

Zanella R, Giorgio S, Shin C-H, Henry CR, Louis C (2004) Characterization and reactivity in CO oxidation of gold nanoparticles supported in TiO2 prepared by deposition-precipitation with NaOH and urea. J Catal 222:357–367

Zhang G, Yang D, Sacher E (2007) Structure and morphology of Co nanoparticles deposited onto highly oriented pyrolytic graphite. J Phys Chem 111:17200–17205

Zhang H, Fu Q, Yao Y, Zhang Z, Ma T, Tan D, Bao X (2008) Size-dependent surface reactions of Ag nanoparticles supported on highly oriented pyrolytic graphite. Langmuir 24:10874–10878

Zubkov T, Morgan GA, Yates JT Jr (2002) Spectroscopic detection of CO dissociation on defect sites on Ru(109): implications for Fischer-Tropsch catalytic chemistry. Chem Phys Lett 362:181–184

Zubkov T, Morgan GA, Yates JT, Kühlert O, Lisowsk M, Schillinger R, Fick D, Jänsch HJ (2003) The effect of atomic steps on adsorption and desorption of CO on Ru(109). Surf Sci 526:57–71